This is a preprint, the final version is subject to change, of the American Mineralogist (MSA)
Cite as Authors (Year) Title. American Mineralogist, in press.
(DOI will not work until issue is live.) DOI: http://dx.doi.org/10.2138/am.2013.4449

Corrected: American Mineralogist , May 6, 2013

Effects of fluid and melt density and structure on high pressure and temperature experimental studies of hydrogen isotope partitioning between coexisting melt and aqueous fluid

Bjorn Mysen
Geophysical Laboratory
Carnegie Instn. Washington
5251 Broad Branch Rd., NW
Washington DC 20015

Abstract

Hydrogen isotope partitioning (as H_2O and D_2O) between silicate-saturated aqueous fluid and water-saturated aluminosilicate melt has been determined with vibrational spectroscopy (Raman and infrared) *in-situ* with the samples at high temperature and pressure by using a hydrothermal diamond anvil cell (HDAC) for sample containment. In order to assess the effects of pressure and, therefore, different silicate speciation in fluids and melts, on the D/H partitioning behavior, two pressure/temperature experimental trajectories (450-800°C/155-754 MPa, and 450°-800°C/562-1271 MPa) were used. In these temperature and pressure ranges, the fluid/melt partition coefficients are temperature (and pressure) dependent with the average enthalpy change, ΔH = -6.6±15 kJ/mol and -10.3±1.1 kJ/mol for H_2O and D_2O, respectively. The ΔH-values for the lower-pressure trajectory (and, therefore, lower fluid density) were 15-20% higher than for the higher-pressure (and higher fluid density) trajectory. The (D/H) ratios of fluids and melts, $(D/H)^{fluid}$ and $(D/H)^{melt}$, are also temperature dependent with a small negative ΔH for $(D/H)^{fluid}$ (average: -2.4±0.8 kJ/mol) and a positive ΔH-value for $(D/H)^{melt}$ (2.3±1.4 kJ/mol). The (D,H) exchange equilibrium between fluid and melt is also temperature (and pressure) dependent so that for the low-density P/T trajectory, the ΔH=-4.2±0.6 kJ/mol, whereas for the higher-density trajectory, ΔH=-5.4±0.7 kJ/mol. The difference between the H_2O and D_2O fluid/melt partition coefficients and the temperature and pressure-dependent D/H fractionation behavior in and between hydrous silicate melts and silicate-saturated aqueous fluid in part is because pressure increases with increasing temperature in the HDAC experiments and the

This is a preprint, the final version is subject to change, of the American Mineralogist (MSA)
Cite as Authors (Year) Title. American Mineralogist, in press.
(DOI will not work until issue is live.) DOI: http://dx.doi.org/10.2138/am.2013.4449

volume difference between fluid and melt differ for H_2O and D_2O. In addition, the silicate speciation in fluids and melts are temperature- and pressure-dependent, which also leads to significantly temperature- and pressure-dependent D/H fractionation within and between silicate melts and fluids at high temperature and pressure. In the Earth's deep crust and upper mantle, hydrogen isotope partitioning between condensed phases and aqueous fluid can differ substantially from that between condensed phases and pure H_2O because the aqueous fluid in the Earth's interior is a concentrated silicate solution wherein the silicate speciation affects the isotope partitioning.

Introduction

Stable isotope (H, C, O, N, S) fractionation is a tool with which to model gas fluxing, degassing, and other materials transport in geological processes (e.g., Pineau et al., 1998; Hauri, 2002; Deines, 2002; Manning, 2004). Such modeling depends on isotope fractionation factors. Theoretical modeling relies on assumptions of no interaction between functional groups in the materials (such as in a gas phase, e. g., Niki et al., 1965; Richet and Bottinga, 1977). In aqueous solutions with strong intermolecular forces (as much as ~20 kJ/mol for hydrogen bonding, for example; Walrafen et al., 1996) this assumption fails (e. g., O' Neil and Truesdell, 1993; Horita et al., 1995; Foustoukos and Mysen, 2012). Furthermore, in silicate melts, whether water-bearing or anhydrous, there are interconnected structural units with bond energies of tens to hundreds of kJ/mol (Bockris and Reddy, 1970; Poole et al., 1995). Type and proportions of such structural units may govern the structural role of protons and deuterons, for example (Cody et al., 2005; Wang et al., 2011). Similar structural features describe silicate solute in aqueous solutions and high

This is a preprint, the final version is subject to change, of the American Mineralogist (MSA)
Cite as Authors (Year) Title. American Mineralogist, in press.
(DOI will not work until issue is live.) DOI: http://dx.doi.org/10.2138/am.2013.4449

temperature and pressure (e.g., Zotov and Keppler, 2002; Mibe et al., 2008; Newton and Manning, 2008). Such structural constraints can affect element and isotope partitioning between melts, fluids, and other phases (O' Neil and Truesdell, 1993; Horita et al., 1995; Driesner and Seward, 2000; Mysen, 2012, 2013).

Isotope partitioning has been determined experimentally by analyzing melts and fluids in experimental charges following their physical separation after quenching of an experiment to ambient temperature and pressure (Kuroda et al., 1982; Dobson et al., 1989; Pineau et al., 1998). The separation process is, however, challenging because during temperature-quenching of hydrous silicate systems, oxide components dissolved in aqueous fluids at high temperature and pressure tend to precipitate (Schneider and Eggler, 1984; Mysen and Wheeler, 2000). This quench precipitation alters the composition of the fluid from its equilibrium values and likely also alters the isotope ratio of the residual fluid because isotope fractionation varies with solute concentration in the fluid (O'Neil and Truesdell, 1993; Horita et al., 1995). The precipitates formed in this manner often cannot be separated completely from coexisting glass or crystals, which renders a major challenge recombination of residual fluid and quenched oxide components to that which existed at high temperature and pressure. Additional complexity can arise from water dissolved in melts at high pressure and temperature because some of this water often exsolves from the melt during cooling of melt to a glass for ambient-condition study. This exsolution process results in water contents of quenched hydrous glass that differ from their high temperature and pressure equilibrium values (Yoder et al., 1957; Eggler and Burnham, 1984). Water exsolution likely also

This is a preprint, the final version is subject to change, of the American Mineralogist (MSA)
Cite as Authors (Year) Title. American Mineralogist, in press.
(DOI will not work until issue is live.) DOI: http://dx.doi.org/10.2138/am.2013.4449

leads to different isotope ratios of the quenched glass compared with the values at high temperature and pressure prior to quenching.

Experimental barriers caused by temperature- and pressure-quenching of experimental charges before analysis can be avoided completely by analysis of the samples *in-situ* while at the temperature and pressure of interest. In this report, the behavior of deuterium and hydrogen has been evaluated in this manner. To this end, the D/H ratios in coexisting melt and fluid, D and H partitioning between them, and D/H exchange equilibria between fluid and melt have been determined by using vibrational spectroscopy to probe samples *in-situ* at high temperature and pressure contained in an externally-heated hydrothermal diamond anvil cell (Bassett et al., 1996). Two different pressure-/temperature-trajectories were explored. In this manner, effects of total water content of melts and of silicate content of coexisting fluid on D/H partitioning between silicate-saturated aqueous fluid and water-saturated silicate melts were evaluated without results being affected by alteration of melts and fluid during temperature-/pressure-quenching of an experiments before isotope analysis.

Experimental Methods

Starting material was the NA10 composition glass originally used by Mysen (2007). This melt has NBO/T=0.5 and Al/(Al+Si)=0.189, which are reasonable approximations to melt polymerization and Al/(Al+Si)-values of island arc andesitic magmas (NBO/T: nonbridging oxygen per tetrahedrally coordinated cations; see Table 1 for description of NBO/T calculation of melt and glass from chemical composition). This composition also has a sufficiently low liquidus temperature and glass transition temperature so that

This is a preprint, the final version is subject to change, of the American Mineralogist (MSA)
Cite as Authors (Year) Title. American Mineralogist, in press.
(DOI will not work until issue is live.) DOI: http://dx.doi.org/10.2138/am.2013.4449

104 examination of melt+fluid equilibria is feasible over a large temperature interval below
105 the practical temperature maximum of an externally-heated diamond anvil cell (≤1000°C
106 – Bassett et al., 1996).

107 Small glass chips (<100 μm across) were loaded together with a D_2O+H_2O (50:50 by
108 volume) liquid, ^{13}C diamond chips (to monitor pressure), and Pt metal (to enhance
109 equilibration rates – see Horita, 1988) in the 500μm central hole of 125 μm thick Ir
110 gaskets used in the diamond cell (Fig. 1). During an experiment, this diameter shrank to
111 ~400 μm and the gasket to ~80-90 μm thickness.

112 The hydrothermal diamond anvil cell (HDAC) was heated with two Mo-wound
113 furnaces (0.1 mm diameter Mo wire) surrounding the upper and lower diamond,
114 respectively. Temperature was measured (and controlled) with K-type thermocouples to
115 within ±1°C. Pressure was generated by the fluid because as temperature is increased and
116 sample volume is kept constant by using the method to ascertain constant sample volume
117 as described by Bassett et al. (1996). Under the assumption that the PVT properties of
118 silicate-saturated mixed (D_2O+H_2O) fluid are the same as those of pure H_2O, pressure can
119 be calculated at any temperature. However, these assumptions can lead to erroneous
120 pressure estimates (e.g., Mysen, 2010), and an independent pressure sensor, therefore,
121 was employed. This was accomplished by monitoring the one-phonon Raman shift of
122 synthetic ^{13}C diamond (Schiferl et al., 1997; Mysen and Yamashita; 2010). Spectrometer
123 positional precision is critical, therefore, to minimize pressure uncertainty. This precision
124 was optimized by using 2400 gratings/mm and Ne emission lines as internal frequency
125 reference. The uncertainty in frequency of the ^{13}C diamond one-phonon-shift then is
126 about ±0.1 cm^{-1}. From the calibration curve of Mysen and Yamashita (2010), this

This is a preprint, the final version is subject to change, of the American Mineralogist (MSA)
Cite as Authors (Year) Title. American Mineralogist, in press.
(DOI will not work until issue is live.) DOI: http://dx.doi.org/10.2138/am.2013.4449

127 frequency precision results in ±40 cm^{-1} precision of pressure. The calibration itself does,
128 however, carry an approximately ±100 MPa error so that the combined uncertainty in the
129 pressure from the one-phonon Raman shift of the ^{13}C diamond is about ±110 cm^{-1}.

130 Platinum was added to the sample chamber because Pt enhances isotope exchange
131 rate (Horita, 1988). For example, D/H equilibrium between liquid H_2O and H_2 at 25°C
132 and ambient pressure is reached within 1-2 hrs (Horita, 1988). Results of time studies of
133 D/H partitioning between fluid and melts using similar compositions and temperature, but
134 higher pressures also indicate that an hour is sufficient to reach isotopic equilibrium
135 (Mysen, 2013).

136 Whether or not the presence of Pt result in dissociation of H_2O to form H_2 and
137 platinum oxide or iridium oxide was assessed by subjecting H_2O in contact with Pt and in
138 Ir gaskets to 400°-800°C/660-1440 MPa by using an HDAC design identical to those
139 under which the D/H partitioning experiments were carried out. There is no evidence of
140 H_2 in the H_2O even at the highest temperatures and pressures (Fig. 3). This result likely is
141 because Pt- and Ir oxides are not stable under these experimental conditions.

142 Coexisting melt and fluid were probed *in-situ* while the samples were at the
143 temperatures and pressures of interest by using a JASCO™ model IMV4000 microFTIR
144 and with an NRS-3100 confocal microRaman spectrometer. Transmission infrared
145 spectroscopy was conducted with 10X objective and condenser cassegraine lenses,
146 an MCT detector, CaF_2 beam splitter and a halogen light source. It should be noted
147 that for the infrared absorption spectroscopy of melt globules in a matrix of silicate-
148 saturated fluid, there often was some interference on spectra of melt from its
149 surrounding aqueous fluid. This interference was because the globule-diameter

150 frequently was less than the distance between the diamond culets (sample
151 thickness; 80-90 μm). When recording the absorption spectra under such
152 circumstances (as illustrated schematically in Fig. 2), the infrared beam will pass
153 through both melt and fluid during measurement. The absorption signal will,
154 therefore, comprise contributions from both melt and fluid.

155 Raman spectroscopic measurements were carried out with a 532 nm laser operating at
156 ~ 7 mW at the sample. Spectra were recorded through a 50X magnification/0.42 N.A.
157 long-working distance Mitutoyo™ objective lens. An Andor™ Model DV401-F1
158 1024x128 pixel (25 μm pixel size) Peltier-cooled CCD was used for signal detection. The
159 spectrometer has a single monochromator, a holographic notch filter, and holographic
160 gratings with 600, 1200, and 2400 gratings/mm available for use. For the measurements,
161 600 gratings/mm were used, which results in a CCD energy window corresponding to ~
162 3650 cm^{-1}. The frequency uncertainty with 600 gratings/mm is ±3-4 cm^{-1}. For the Raman
163 spectroscopic measurements of ^{13}C diamond used for pressure estimates, 2400
164 gratings/mm were employed with Ne emission lines used for internal frequency
165 calibration, which result in the frequency uncertainty is ±0.1 cm^{-1} discussed in more
166 detail above. The diameter of the laser beam at the sample was ~ 1 μm. The sample
167 excitation volume extends to 10-20 μm depth for transparent samples such as fluid and
168 melt. The Raman measurements do not suffer from the same interference issues that
169 affected the infrared absorption measurements because of the much smaller sample
170 volume probed with the Raman spectroscopy compared with FTIR absorption
171 spectroscopy,.

This is a preprint, the final version is subject to change, of the American Mineralogist (MSA)
Cite as Authors (Year) Title. American Mineralogist, in press.
(DOI will not work until issue is live.) DOI: http://dx.doi.org/10.2138/am.2013.4449

In each of the two pressure/temperature series of Raman and infrared measurements, the sample was first brought to the highest temperature (800°C) and corresponding pressure (1271 and 754 MPa for high-density and low density fluid, respectively; see below for further detail). Following Raman spectroscopic measurements of the carbon-13 diamond, of diamond in the diamond cell itself, of fluid, and of melt at this temperature (and pressure), the temperature was decreased at 1°C/s to successively lower temperatures and then kept for approximately an hour at each of the desired temperature and pressure conditions (Table 2) followed by the same sequence of spectroscopic measurements. The same sample was, therefore, used for all temperatures and pressures in each of the two series of Raman and infrared measurement. In order to remove the interference from the 2nd order diamond shift, Raman spectra of diamonds recorded at the same temperature as the spectra of samples, were subtracted from the spectra of fluids and melts.

The infrared spectroscopic measurements were conducted subsequent to Raman measurements, and using the same sample and with the same temperature/pressure path as in the Raman spectroscopy. It was assumed that the pressures during the infrared measurements were the same as those during the Raman measurements. Absorption spectra of an empty cell after measurements were recorded at the same temperatures in order to normalize out the effect of diamond absorption on the infrared spectra.

Results

This is a preprint, the final version is subject to change, of the American Mineralogist (MSA)
Cite as Authors (Year) Title. American Mineralogist, in press.
(DOI will not work until issue is live.) DOI: http://dx.doi.org/10.2138/am.2013.4449

The temperature-dependent P/T paths of the two series of experiments with different fluid densities (termed low density and high density; Fig. 4, see also Table 2) were:

$$P_{low\ density} = 573 - 2.29 \bullet T(^{\circ}C) + 0.00313 \bullet T^2, \quad (1a)$$

and

$$P_{high\ density} = 24 + 0.999 \bullet T(^{\circ}C) + 0.000671 \bullet T^2. \quad (1b)$$

The pressure/temperature relations calculated with the assumption that the fluid density in the experiments can be modeled with that of pure H_2O (Wagner and Pruss, 2002) are also shown in Fig. 4. There is difference between the trajectories derived with this method compared with that from the one-phonon shift of carbon-13 diamond (Fig. 4) exists because silicate components are dissolved in the fluid (Manning, 1994; Newton and Manning, 2008). These solutes affect PVT properties of the aqueous fluid (Mysen, 2010). Furthermore, PVT properties of D_2O fluid as compared with pure H_2O (Bazaev et al., 2003) might also contribute to the difference pressure/temperature trajectories.

Under the conditions investigated, the temperatures exceed that of the glass transition because dissolved water depresses this temperature by several hundred degrees (Duebner et al., 2003; Del Gaudio et al., 2007). Above the glass transition temperature (but not necessarily above the liquidus temperature), the supercooled melt behaves structurally and thermodynamically as a melt (the material is

energetically relaxed). This is not the case for a glass, which is not relaxed (e. g., Moynihan et al., 1976; Scherer, 1986). It follows that the data reported here are quantitatively applicable to those of a melt above its liquidus temperature.

Raman Spectra.

Information on the nature of the aluminosilicate bonding environment (structure) was derived from interpretation of the spectra in the low-frequency range, 200-1200 cm^{-1}. The D_2O and H_2O environments were probed with spectra in the high-frequency range between about 2500 and 3800 cm^{-1}.

In the low-frequency range, the Raman spectra of hydrous melts characteristically have broad bands in the 300-600 cm^{-1} and 800-1200 cm^{-1} frequency ranges (Fig. 4). This topology remains at all temperatures and pressures under study here. These features are typical of alkali aluminosilicate glass and melt spectra whether these materials are anhydrous or hydrous (e.g., McMillan et al., 1992; Mysen, 2007; Malfait et al., 2007).

With increasing temperature and pressure, there is intensity growth centered near 500 and 850 cm^{-1} (marked "a" and "b", respectively, in Fig. 5). The intensity near 500 cm^{-1} is assigned to bending and rocking (Si, Al)-O vibrations in depolymerized structural units. The abundance of these structural units increases, therefore, with increasing temperature and pressure (which also results in increasing water solubility in silicate melts; see McMillan, 1994, for review). The intensity, "b" (Fig. 5), likely could be assigned to Si-OH stretching (near 970 cm^{-1};

238 e.g. Stolen and Walrafen, 1976), Si-OD stretching (near 900 cm^{-1}; McMillan et al.,
239 1993), and $Si\text{-}O^-$ stretching in Q^2 species (near 950 cm^{-1}; Mysen, 2007).

240 The low-frequency range in Raman spectra of silicate-saturated fluid differs
241 from the spectra of hydrous melts in that its dominant intensity is near 770 cm^{-1}
242 instead of the lower- and higher-frequency intensity maxima in the spectra of
243 hydrous melts (Figs. 5 and 6). This frequency is identical to that in spectra of fluids
244 in Al-free silicate systems (Zotov and Keppler, 2002; Mysen, 2009). In the spectra of
245 low-density fluid, the 770 cm^{-1} band is the only discernible Raman signal (Fig. 6A),
246 whereas in the spectra of high-density fluid (where the pressure at given
247 temperature is twice or more than that of low-density fluid; Table 2) there is
248 intensity growth near 600 cm^{-1} (marked "a" in Fig. 6B). At the highest
249 temperatures and pressures there is also a shoulder on the high-frequency side of
250 the 770 cm^{-1} band (marked "b" in Fig. 6B).

251 The 770 cm^{-1} band (Fig. 6) in Raman spectra of silicate-saturated aqueous fluids
252 is assigned to $Si\text{-}O^-$ stretching in Q^0 units (e.g., Zotov and Keppler, 2002; Mibe et al.,
253 2008). In the low-density fluid, the only detectable silicate species is, therefore, Q^0
254 (isolated SiO_4 tetrahedra). In the high-density fluids, on the other hand, the
255 additional Raman intensity on the low- and high-frequency side of the 770 cm^{-1}
256 band is because more polymerized structural units of silicate in the high-density
257 fluid. The shoulder near 820-830 cm^{-1} ("b" in Fig. 6B) is assigned to $Si\text{-}O^-$
258 stretching in Q^1-species and the intensity maximum marked "a" in Fig. 5b most
259 likely is due to Si-O-Si bending motion of the same species (e.g., Zotov and Keppler,
260 2002; Mibe et al., 2008).

In the high-frequency range, the Raman spectra are dominated by intensity envelopes in the 2500-2700 cm^{-1} and 3200-3700 cm^{-1} ranges, respectively (shown with gradient fill and light gray fill in Fig. 7). The envelope between 3200 and 3700 cm^{-1} is a comparatively featureless broad asymmetric band that evolves toward a single, symmetric band with increasing temperature (and pressure). This evolution is similar to that in spectra of aqueous fluids and hydrous melts in other systems (Kohl et al., 1991; Frantz et al., 1993; Kawamoto, 2004). The bands that comprise this intensity envelope are assigned to OH vibrations in molecular H_2O and in HDO (c) and to OH vibrations in OH-groups that are bonded to metal cations (i. e., Si^{4+}, Al^{3+}, and perhaps Na^{+}; Mysen and Virgo, 1986; Cody et al., 2005). The temperature-dependent evolution of this intensity envelope toward a single symmetric band reflects diminishing extent of hydrogen bonding with increasing temperature (Walrafen et al., 1986; Frantz et al., 1993; Foustoukos and Mysen, 2012).

The 2500-2800 cm^{-1} intensity envelope comprises bands that are assigned to O ···D vibrations in molecular D_2O and HDO, and in OD groups bonded to metal cations (see, for example, Walrafen, 1971; Max and Chapados, 2002; Foustoukos and Mysen, 2012). There is considerably more topological variation in this intensity envelope than in the higher-frequency envelope comprising O...H vibrations (Fig. 7). The two highest-frequency bands, near 2650 and 2550 cm^{-1}, respectively, are assigned to OD groups that form bonding with Si^{4+} and Al^{3+} (Walrafen, 1971; Max and Chapados, 2002). There is, in addition, a third band near 2450 cm^{-1}, which is more intense in spectra of melts than in spectra of fluids (marked "b" in the examples in Fig. 7). It is possible that

this band can be assigned to OD stretching in OD groups bonded to Na^+. The relative intensities of these groups of bands differ in the spectra of melts and fluids (Fig. 7).

Finally, there are two bands (at 2910 and 2970 cm^{-1}) observed in all spectra of fluid, but that are not seen in spectra of melts (marked "a" in Fig. 7). There are several possible assignments of these bands. This frequency range is, for example, that where bands assignable to C..H stretching in organic functional groups (e.g., Socrates, 2001). It is also where D..D vibrations in D_2 would occur (e.g., Veirs and Rosenblatt, 1987; Socrates, 2001). However, the assignment to D_2 is highly unlikely because there is no evidence of H_2 (dominant Raman bands near 4150 cm^{-1}) or HD (sharp band near 3620 cm^{-1}; Williams et al., 2002). The first alternative implies interaction of the H_2O+D_2O fluid with carbon in the sample area. For example, it could be a reaction between H_2O and carbon in the diamond of the HDAC to form CH_4 (Chou and Anderson, 2009). Another possible source of the carbon is incomplete removal of a residue of organic solvents from cleaning of gaskets after polishing. Whatever the source of carbon, the band near 2900 cm^{-1} could be assigned to C-H stretching in CH_4 or methyl (CH_3) groups and the 2960 cm^{-1} band to C-H stretching in CH_xD_y isotopologues (Foustoukos and Mysen, 2013). The latter isotopologues were then formed by interaction with deuterium in the D_2O.

Infrared Absorption Spectra

Infrared absorption spectra were recorded between 2000 and 7800 cm^{-1}. The two dominant regions are centered near 2600 and 3500 cm^{-1} (gradient-filled and gray

fill, respectively; see Fig. 8). In addition, there are much weaker bands near 4500, 5200 and, sometimes, 7000 cm^{-1} (see inserts, Fig. 8).

The principal contribution to the 2600 cm^{-1} maximum is absorption by OD groups in molecular D_2O and from OD-groups forming bonds with metal cations (Bukka et al., 1992; Martra et al., 2001). The equivalent OH absorptions result in the other main peak centered near 3500 cm^{-1} (e.g., Stone and Walrafen, 1982). In addition, possible combination bands of OD/SiOD and OD/SiOH, computed by linear combination of the OD fundamental stretching at 2600 cm^{-1}, SiOH near 970 and SiOD near 900 cm^{-1}, can result in absorption bands in the 3500-3600 cm^{-1} frequency region of the infrared spectra (see also Stone and Walrafen, 1982). If present, the intensity contributions from these peaks cannot be isolated quantitatively from the intensity assigned to fundamental OH stretch. It is proposed, for example, that the peak marked "b" could contain this contribution (Fig. 8).

The much weaker bands near 4500 and 5000 cm^{-1} (Fig. 8) commonly are interpreted to be combination bands involving OH-groups and H_2O, respectively (e.g., Stolper, 1982; Behrens and Nowak, 2003). It is possible, however, that a peak marked "a" in the inserts in Fig. 8 could be the first overtone of molecular D_2O (Walrafen et al., 1996). That notwithstanding, the much grater OH/H_2O ratio in hydrous melts as compared with coexisting, silicate-saturated aqueous fluid is visually evident (Fig. 8).

Discussion

This is a preprint, the final version is subject to change, of the American Mineralogist (MSA)
Cite as Authors (Year) Title. American Mineralogist, in press.
(DOI will not work until issue is live.) DOI: http://dx.doi.org/10.2138/am.2013.4449

Water and heavy water exist in melts and fluids in the form of OH and OD groups that form bonds with silicate components and as molecular H_2O (shown with the symbol H_2O^o here) and molecular D_2O (shown as D_2O^o). The Raman scattering and infrared absorption from these two groups of species may be used to extract D and H partitioning between fluids and melts. To this end, the ratios of integrated area of the intensity envelopes near 2600 cm^{-1} and 3500 cm^{-1} in the Raman and FTIR spectra (Figs. 7 and 8), assigned to vibration of OD- and OH-bearing species, whether bonded to metal cations or protons, respectively, can be used as a measure of concentration ratios of OD- and OH-containing species, respectively, provided that the force constants of OD and OH stretching are the same. Mysen (2013) concluded that this is so, which means that these force constants cancel out and, therefore, the ratio of integrated areas equals the abundance ratio of deuterated and pronated species. These concentration ratios are equivalent to total D and H concentration ratios in the samples because there is no evidence for other H- or D-bearing species. Therefore, it follows from the Raman spectra;

$$D/H = X_{OD+(D2O)}^{o}/X_{OH+(H2O)}^{o} = A_{OD}/A_{OH}. \quad (2)$$

In eqn. (2), $X_{OD+(D2O)}^{o}$ and $X_{OH+(H2O)}^{o}$ are the sum of concentrations of structurally bound OD and molecular D_2O and OH and molecular H_2O. The A_{OD} and A_{OH} are the integrated areas of Raman frequencies centered near 2600 and 3500 cm^{-1}, respectively (Fig. 8). In equation (2), it is assumed that the force constants for OD and OH stretching are the same in all environments so that the ratio of integrated areas,

This is a preprint, the final version is subject to change, of the American Mineralogist (MSA)
Cite as Authors (Year) Title. American Mineralogist, in press.
(DOI will not work until issue is live.) DOI: http://dx.doi.org/10.2138/am.2013.4449

350 A_{OD}/A_{OH}, equals the abundance ratio, $X_{OD+(D2O)}^{o}/X_{OH+(H2O)}^{o}$. Mysen (2013) found this
351 assumption accurate within the error of the data (~5 %) by measuring the ratios of
352 integrated areas, A_{OD}/A_{OH}, for supercritical fluids with known $X_{OD+(D2O)}^{o}/X_{OH+(H2O)}^{o}$.
353 The deuterium and proton partition coefficients between fluid and melt derived
354 from the Raman spectra are;
355
356 $$K_D^{fluid/melt} = X_{OD+(D2O)}^{o\ fluid}/X_{OD+(D2O)}^{o\ melt} = A_{OD}^{fluid}/A_{OD}^{melt}, \quad (3a)$$
357
358 and
359
360 $$K_H^{fluid/melt} = X_{OH+(H2O)}^{o\ fluid}/X_{OH+(H2O)}^{o\ melt} = A_{OH}^{fluid}/A_{OH}^{melt}. \quad (3b)$$
361
362 No additional assumptions are needed.
363 For infrared absorption spectra, molecular weights of D_2O and H_2O and density
364 of fluid and melt must be integrated into the calculations. By using the Beer-Lambert
365 law simply to describe a relationship between total H_2O and D_2O and the absorption
366 intensities, the (D/H)-ratio from the FTIR absorption spectra is;
367
368 $$(D/H) = X_{OD+(D2O)}^{o}/X_{OH+(H2O)}^{o} = (A_{OD}/A_{OH}) \bullet 20.02/18.02, \quad (4)$$
369
370 where 20.02 and 18.02 are molecular weights of D_2O and H_2O, respectively. The
371 fluid/melt partition coefficients are;
372

This is a preprint, the final version is subject to change, of the American Mineralogist (MSA)
Cite as Authors (Year) Title. American Mineralogist, in press.
(DOI will not work until issue is live.) DOI: http://dx.doi.org/10.2138/am.2013.4449

373 $K_D^{fluid/melt} = X_{OD+(D2O)}{}^{o\ fluid}/X_{OD+(D2O)}{}^{o\ melt} = (A_{OD}^{fluid}/A_{OD}^{melt}) \bullet (d^{melt}/d^{fluid})$, (5a)

374

375 and

376

377 $K_H^{fluid/melt} = X_{OH+(H2O)}{}^{o\ fluid}/X_{OH+(H2O)}{}^{o\ melt} = A_{OH}^{fluid}/A_{OH}^{melt} \bullet (d^{melt}/d^{fluid})$, (5b)

378

379 where d^{melt} and d^{fluid}, are the density of melt and fluid, respectively.

380 In equations (4) and (5), it is assumed that the molar absorption coefficients for
381 total H_2O and total D_2O do not vary with concentration of water and heavy water,
382 respectively, and that their values are equal so that these cancel out in eqns. (4) and
383 (5). The ratio of structurally bound OH-groups to molecular water, OH/H_2O^o, in
384 melts is insensitive to total H_2O at concentration higher than 5-6 wt% (Dixon and
385 Stolper, 1995; Zotov and Keppler, 1998). The water solubility in the present melts is
386 not known with precision. However, by using the empirical water solubility model
387 of Moore et al. (1998), an H_2O content ≥5 wt% in these melts is approximately
388 correct for the lowest temperature and pressure and increases with increasing
389 temperature and pressure. The OH/H_2O^o ratio, therefore, is not expected to vary
390 much in the temperature and pressure ranges studied. Less is known about the
391 behavior of heavy water. It is assumed, therefore, that the D_2O solubility and the
392 OD/D_2O^o ratio are similar to those of H_2O.

393 The density of fluid and melt is also needed in equation (5). Fluid density was
394 derived from the intersection of a fluid isochore with the fluid+vapor univariant
395 curve and using the PVT data of pure H_2O to determine the corresponding density

This is a preprint, the final version is subject to change, of the American Mineralogist (MSA)
Cite as Authors (Year) Title. American Mineralogist, in press.
(DOI will not work until issue is live.) DOI: http://dx.doi.org/10.2138/am.2013.4449

(Wagner and Pruss, 2002). It is assumed, therefore, that the density of a silicate-saturated mixed H_2O+D_2O fluid can be modeled with the properties of pure H_2O. This assumption leads to a density uncertainty. This uncertainty increases with increasing temperature and pressure and may be as high as 10 % at the highest temperatures and pressures because of the increased silicate solubility in aqueous fluids with increasing temperature and pressure (see Mysen, 2010). These differences from the PVT behavior of pure H_2O are also reflected the different pressure/temperature trajectories in Fig. 4.

The density of coexisting water-saturated hydrous melt is also temperature- and pressure-dependent. This is in part because of temperature- and pressure-dependent thermal expansion and compressibility and in part because the solubility of water in melts increases with increasing pressure. By using the partial molar volumes of oxides in silicate melts from Lange (1994), water solubility estimates from Moore et al. (1998), and a partial molar volume of H_2O of 12 cm^3/mol (Richet et al., 2000), the melt density is 2.2±0.2 g/cm^3 in the pressure/temperature range of the experiments. This value was used in equation (5).

The fluid/melt partition coefficient, $K_H^{fluid/melt}$, differs from that of $K_D^{fluid/melt}$ at all temperatures, pressures, and fluid densities (Figs. 9 and 10). The ΔH-value, obtained from the slope of the relationships between ln $K_H^{fluid/melt}$ vs. 1/T and ln $K_D^{fluid/melt}$ vs. 1/T (Figs. 9 and 10), is essentially the same whether from Raman or FTIR data (Table 3). We note, however, that the curves for the FTIR spectra are offset to higher partition coefficient values compared with those determined from the Raman spectra (Figs. 9 and 10). This offset could be because of too high melt density or too

This is a preprint, the final version is subject to change, of the American Mineralogist (MSA)
Cite as Authors (Year) Title. American Mineralogist, in press.
(DOI will not work until issue is live.) DOI: http://dx.doi.org/10.2138/am.2013.4449

low fluid density when calculating the K_D and K_H-values with equation (5). An error of 20-25% in the fluid/melt density ratio is necessary to reach agreement between the partition coefficients from the two different spectroscopic measurements. This is larger than the error introduced by the uncertainty in the density estimates. It is likely, therefore, that at least a portion of the difference is because there are contributions other than OD and OH stretch vibrations to each of the two main absorption envelopes at 2600 and 3500 cm^{-1}.

The ΔH for the D_2O partitioning is about twice that of H_2O, which may suggest partial molar volume differences between H_2O and D_2O in melt and fluid (partial molar volume of H_2O and D_2O in aqueous brines do indeed differ, see for example; Trevani et al., 2007) because pressure increases with temperature in these experiments. A volume effect might contribute to the slightly different ΔH-values in the two experimental series with different fluid density (Figs. 4, 9, 10; Table 3). With different partial molar volumes of D_2O and H_2O in melts and fluids, their pressure derivatives likely also are different. Therefore, the volume difference, $\Delta V^{fluid\text{-}melt}$, for H_2O and D_2O are not the same and the difference is pressure-dependent. The different ΔH-values may also be due to variations in silicate, water, and heavy water speciation in melts and fluids, or contributions from all these factors.

It follows from the temperature-dependent $K_D^{fluid/melt}$ and $K_H^{fluid/melt}$ that $(D/H)^{fluid}$ and $(D/H)^{melt}$ are also temperature (and pressure dependent; see Fig. 11). However, the behavior differs for melt and fluid with $(D/H)^{fluid}$ decreasing with increasing temperature, whereas for $(D/H)^{melt}$, the temperature correlation is positive (Fig. 11). The slope from the high-density FTIR data yields a ΔH-value in the same range as that obtained with the

This is a preprint, the final version is subject to change, of the American Mineralogist (MSA)
Cite as Authors (Year) Title. American Mineralogist, in press.
(DOI will not work until issue is live.) DOI: http://dx.doi.org/10.2138/am.2013.4449

Raman data, but the error is very large because of the data scatter (see above for discussion of this). The ΔH derived from the temperature relationships of $(D/H)^{fluid}$ is slightly greater for the low-density than for high-density fluid (Fig. 11A; Table 3). This difference likely is because in the low-density fluid, the only silicate-species is Q^0 over the entire temperature and pressure range, whereas for the high-density fluid, additional Q-species are formed at the higher temperatures and pressures. In this regard the high-density data resemble the even high-density fluid experiments by Mysen (2013) (see also Fig. 4). In contrast, the $(D/H)^{melt}$ increases with increasing temperature (Fig. 11B) with the ΔH of $(D/H)^{melt}$ slightly less temperature-dependent in the experiments where melt coexists with low-density fluid than when with high-density fluid (Table 3). Because the pressure/temperature trajectories of the two experimental series experiments differ, so does the solubility of water in the melt. That, in turn, causes changes in abundance trajectories of Q-species along the different pressure/temperature paths, which, in turn, appear to change the details of how water and heavy water interact with the silicate melt.

The D/H exchange equilibrium constant, $K_{D/H}^{fluid/melt}$, for,

$$H_2O(melt) + D_2O(fluid) = D_2O(melt) + H_2O(fluid), \quad (6)$$

where H_2O and D_2O denote total water and heavy water concentration. The equilibrium constant,

$$K_{D/H}^{fluid/melt} = X_{D2O}^{melt} \bullet X_{H2O}^{fluid} / X_{H2O}^{melt} \bullet X_{D2O}^{fluid} = (D/H)^{melt}/(D/H)^{fluid}, \quad (7)$$

is shown as a function of temperature (and pressure) in Fig. 12. Here the mol fractions represent the sum of water and heavy water dissolved in fluids and melts both as OH and OD groups bonded to silicate components and as molecular H_2O^o and D_2O^o.

The (D/H) partitioning relationships (Fig. 12) may be partly because the composition and structure of fluid and melt are temperature and pressure-dependent and, therefore, so is the $(D/H)^{fluid}$ and $(D/H)^{melt}$. In addition, the pressure increase will affect the (D/H)-partitioning in part because, in analogy with D-substituted $Mg(OH)_2$ (Horita et al., 2010), the compressibility and density of D_2O-bearing melt differs from those of H_2O-bearing melt and fluid. In addition, the speciation and abundance of silicate solute in fluid is temperature- and pressure-dependent, which can cause D/H fractionation to vary. The contribution from fluid is silicate concentration dependent, so the higher the fluid density, the more of an influence from the silicate components in aqueous fluid is likely. The resulting difference in D/H fractionation factors is the underlying cause for the temperature/pressure dependence.

The D/H partitioning data reported here and elsewhere (Wang et al., 2011; Mysen, 2013) were obtained in compositionally relatively simple aluminosilicate systems and cannot, therefore, be applied quantitatively to characterization of natural processes. However, the principles that relate silicate speciation in fluids and melts to D/H fractionation are the same whether in chemically simple systems such as studied here or in chemically more complex systems such as those of magmatic liquids and hydrothermal fluids in the crust and the mantle of the Earth.

Acknowledgments

488 This research was supported by NSF grants EAR-0734182 and EAR-1212754.
489

References

Bassett, W. A., T.-C. Wu, I.-M. Chou, T. Haselton, J. D. Frantz, B. O. Mysen, W.-L. Huang, S. K. Sharma, and D. Schiferl (1996), The hydrothermal diamond anvil cell (DAC) and its applications, in Mineral Spectroscopy: A Tribute to Roger G. Burns, edited by M. D. Dyar, C. A. McCammon and M. Schaefer, pp. 261-272, The Geochemical Society, Houston.

Bazaev, A. R., I. M. Abdulagatov, J. W. Magee, E. A. Bazaev, and A. E. Ramazanova (2003), PVTx measurements for H_2O+D_2O mixtures in the near-critical and supercritical regions, Journal of Supercritical Fluids, 26, 115-128.

Behrens, H., and M. Nowak (2003), Quantification of H_2O speciation in silicate glasses and melts by IR spectroscopy - in situ versus quench techniques, Phase Transitions, 76, 45-61.

Bockris, J., and A. K. N. O'M. Reddy (1970), Modern Electrochemistry, 662 pp., Plenum Press, New York.

Bukka, K., J. D. Miller, and J. Shabtai (1992), FTIR study of deuterated montmorillonites: Structural features relevant to pillared clay stability, Clays and Clay Minerals, 40, 92-102

Chou, I.-M., and A. J. Anderson (2009), Diamond dissolution and the production of methane and other carbon-bearing species in hydrothermal diamond anvil cell, Geochimica et Cosmochimica Acta, 73, 6360-6366.

Cody, G. D., B. O. Mysen, and S. K. Lee (2005), Structure vs. composition: A solid state ^{1}H and ^{29}Si NMR study of quenched glasses along the Na_2O-SiO_2-H_2O join, Geochimica et Cosmochimica Acta, 69, 2373-2384.

Deines, P. (2002), The carbon isotope geochemistry of mantle xenoliths, Earth-Science Reviews, 58, 247-278.

Del Gaudio, P., H. Behrens, and J. Duebner (2007), Viscosity and glass transition temperature of hydrous float glass, Journal of Non-Crystalline Solids, 353, 223-236.

Dixon, J. E., and E. M. Stolper (1995), An experimental study of water and carbon dioxide solubilities in mid-ocean ridge basaltic liquids; Part II, Applications to degassing, Journal of Petrology, 36, 1633-1646.

Dobson, P. F., S. Epstein, and E. M. Stolper (1989), Hydrogen isotope fractionation between coexisting vapor and silicate glasses and melts at low pressure, Geochimica et Cosmochimica Acta, 53, 2723-2731.

Driesner, T., and T. M. Seward (2000), Experimental and simulation study of salt effects and pressure/density effects on oxygen and hydrogen stable isotope liquid-vapor fractionation for 4–5 molal aqueous NaCl and KCl solutions to 400°C, Geochimica et Cosmochimica Acta, 64, 1773-1784.

Duebner, J., R. Müller, H. Behrens, and G. Heide (2003), Water and the glass transition temperature of silicate melts, Journal of Non-Crystalline Solids, 330, 268-273.

Eggler, D. H., and C. W. Burnham (1984), Solution of H_2O in diopside melts: a thermodynamic model, Contributions to Mineralogy and Petrology, 85, 58-66.

Foustoukos, D. I., and B. O. Mysen (2012), D/H isotopic fractionation in the H_2-H_2O system at supercritical water conditions: Composition and hydrogen bonding effects, Geochimicia et Cosmochimica Acta, 86, 88-102.

Foustoukos, D. I., and B. O. Mysen (2013), Condensed-phase isotope effects on H/D methane isotopologues dissolved in supercritical aqueous solutions, American Mineralogist **in press**.

Frantz, J. D., J. Dubessy, and B. Mysen (1993), An optical cell for Raman spectroscopic studies of supercritical fluids and its applications to the study of water to 500 °c and 2000 bar, Chemical Geology, 106, 9-26.

536 Hauri, E. H. (2002), SIMS analysis of volatiles in silicate glasses, 2: isotopes and abundances in
537 Hawaiian melt inclusions, Chemical Geology 183, 115-141.
538 Horita, J. (1988), Hydrogen isotope analyses of natural waters using an H_2-water equilibration
539 method: A special implication to brines, Chemical Geology, 72, 89-94.
540 Horita, J., D. R. Cole, and D. J. Wesolovski (1995), The activity-composition relationship of
541 oxygen and hydrogen isotopes in aqueous salt solutions; III, Vapor-liquid water equilibration
542 of NaCl solutions to 350°C, Geochimica et Cosmochimica Acta, 59, 1139-1151.
543 Horita, J., A. M. dos Santos, C. A. Tulk, B. C. Chakoumakos, and V. B. Polyakov (2010), High-
544 pressure neutron diffraction study on H–D isotope effects in brucite, Physics and Chemistry
545 of Minerals, 37, 741-749.
546 Kawamoto, T., S. Ochiai, and H. Kagi (2004), Changes in the structure of water deduced from
547 the pressure dependence of the Raman OH frequency, Journal of Chemical Physics, 120,
548 5867-5870.
549 Kohl, W., H. A. Lindner, and E. U. Franck. (1991), Raman spectra of of water to 400°C and
550 3000 bar, Berichte Bundesenges Physikalische Chimie, 95, 1586-1593.
551 Kuroda, Y., Y. Kariya, T. Suzukoki, and S. Matsuo (1982), D/H fractionation between water and
552 the melts of quartz, K-feldspar, albite and anorthite at high temperature and pressure,
553 Geochemical Journal, 16, 73-78.
554 Lange, R. A. (1994), The effect of H_2O, CO_2, and F on the density and viscosity of silicate melts,
555 in Volatiles in Magmas, edited by M. R. Carroll and J. R. Holloway, pp. 331-370,
556 Mineralogical Society of America, Washington DC.
557 Malfait, W. J., V. P. Zakaznova-Herzog, and W. E. Halter (2007), Quantitative Raman
558 spectroscopy: High-temperature speciation of potassium silicate melts, Journal of Non-
559 Crystalline Solids, 353, 4029-4042.
560 Manning, C. E. (1994), The solubility of quartz in H_2O in the lower crust and upper mantle,
561 Geochimica et Cosmochimica Acta, 58, 4831-4840.
562 Manning, C. E. (2004), The chemistry of subduction-zone fluids, Earth and Planetary Science
563 Letters, *223*, 1-16.
564 Martra, G., T. Cacciatori, L. Marchese, J. S. J. Hargreaves, I. M. Mellor, R. W. Joyner, and S.
565 Coluccia (2001), Surface morphology and reactivity of microcrystalline MgO: Single and
566 multiple acid–base pairs in low coordination revealed by FTIR spectroscopy of adsorbed CO,
567 CD_3CN and D_2, Catalysis Today, 70, 121-130.
568 Max, J. J., and C. Chapados (2002), Isotope effects in liquid water by infrared spectroscopy,
569 Journal of Chemical Physics, 116, 4626-4642.
570 McMillan, P. F. (1994), Water solubility and speciation models, in Volatiles in Magmas, edited
571 by M. R. Carroll and J. R. Holloway, pp. 131-156, Mineralogical society of America,
572 Washington DC.
573 McMillan, P. F., G. H. Wolf, and B. T. Poe (1992), Vibrational spectroscopy of silicate liquids
574 and glasses, Chemical Geology, 96, 351-366.
575 McMillan, P. F., B. T. Poe, T. R. Stanton, and R. L. Remmele (1993), Raman spectroscopic
576 study of H/D isotopically substituted hydrous aluminosilicate glasses, Physics and Chemistry
577 of Minerals, 19, 454-459.
578 Mibe, K., I. M. Chou, and W. A. Bassett (2008), In situ Raman spectroscopic investigation of the
579 structure of subduction-zone fluids, Journal of Geophysical Research,
580 DOI: 10.1029/2007JB005179
581 Moore, G., T. Vennemann, and I. S. E. Carmichael (1998), An empirical model for the solubility

of H_2O in magmas to 3 kilobars, American Mineralogist , 83, 36-42.
Moynihan, C. T., A. J. Eastal, and M. A. DeBolt (1976), Dependence of the fictive temperature of glass and cooling rate, Journal of the American Ceramic Society, 59, 12-16.
Mysen, B. O. (2007), The solution behavior of H_2O in peralkaline aluminosilicate melts at high pressure with implications for properties of hydrous melts. Geochimica et Cosmochimica Acta, 71, 1820-1834., Geochimica et Cosmochimica Acta, 71, 1820-1834.
Mysen, B. O. (2009), Solution mechanisms of silicate in aqueous fluid and H_2O in coexisting silicate melts determined in-situ at high pressure and high temperature, Geochimica et Cosmochimica Acta, 73, 5748-5763.
Mysen, B. O. (2010), Speciation and mixing behavior of silica-saturated aqueous fluid at high temperature and pressure, American Mineralogist , 95, 1807-1816.
Mysen, B. O. (2012), High-pressure/-temperature titanium solution mechanisms in silicate-saturated aqueous fluids and hydrous silicate melts, American Mineralogist , 97, 1241-1251.
Mysen, B. O. (2013), Hydrogen isotope fractionation between coexisting hydrous melt and silicate-saturated aqueous fluid: An experimental study in situ at high pressure and temperature, American Mineralogist , 98, 376-386.
Mysen, B. O., and D. Virgo (1986), Volatiles in silicate melts at high pressure and temperature. 1. Interaction between OH groups and Si^{4+}, Al^{3+}, Ca^{2+}, Na^{+} and H^{+}, Chemical Geology, 57, 303-331.
Mysen, B. O., and K. Wheeler (2000), Alkali aluminosilicate-saturated aqueous fluids in the Earth's upper mantle, Geochimica et Cosmochimica Acta, 64, 4243-4256.
Mysen, B. O., and S. Yamashita (2010), Speciation of reduced C-O-H volatiles in coexisting fluids and silicate melts determined in-situ to ~1.4 GPa and 800°C. Geochim. Cosmochim, Geochimica et Cosmochimica Acta, 74, 4577-4588.
Newton, R. C., and C. E. Manning (2008), Thermodynamics of SiO_2-H_2O fluid near the upper critical end point from quartz solubility measurements at 10 kbar, Earth and Planetary Science Letters, 274, 241-249.
Niki, H., Y. Rousseau, and G. J. Mains (1965), Hydrogen-Deuterium Exchange Reaction .I. 63pi Mercury Photosensitized, Journal of Physical Chemistry, *69*, 45-52.
O'Neil, J. R., and A. E. Truesdell (1993), Oxygen isotope fractionation studies of solute water interactions, in Stable isotope geochemistry: A tribute to Samuel Epstein, edited by H. P. Taylor, J. R. O'Neil and I. R. Kaplan, pp. 17-25, The Geochemical Society, Calgary.
Pineau, F., S. Shilobreeva, A. Kadik, and M. Javoy (1998), Water solubility and D/H fractionation in the system basaltic andesite--H_2O at 1250°C and between 0.5 and 3 kbars, Chemical Geology, 147, 173-184.
Poole, P. H., P. F. McMillan, and G. H. Wolf (1995), Computer simulations of silicate melts, in Structure, dynamics and properties of silicate melts, edited by J. F. Stebbins, P. F. McMillan and D. B. Dingwell, pp. 563-616, Mineralogical Society of America, Washington DC.
Ratcliffe, C. I., and D. E. Irish (1982), Vibrational studies of solutions at elevated temperatures and pressures. 5. Raman studies of liquid water up to 300 °C., Journal of Physical Chemistry 86, 4897-4905.
Richet, P., Y. Bottinga, and M. Javoy (1977), A review of hydrogen, carbon, nitrogen, oxygen, sulphur, and chlorine stable isotope fractionation among gaseous molecules, Annual Review of Earth and Planetary Sciences5, 65-110.
Richet, P., A. Whittington, F. Holtz, H. Behrens, S. Ohlhorst, and M. Wilke (2000), Water and the density of silicate glasses, Contributions to Mineralogy and Petrology, 138, 337-347.

Scherer, G. W. (1986), Relaxation in Glasses and Composites., John Wiley & Sons, New York.

Schiferl, D., M. Nicol, J. M. Zaug, S. K. Sharma, T. F. Cooney, S.-Y. Wang, T. R. Anthony, and J. F. Fleischer (1997), The Diamond $^{13}C/^{12}C$ Isotope Raman Pressure Sensor System for High Temperature/Pressure Diamond-Anvil Cells with Reactive Samples, Journal of Applied Physics, 82, 3256-3265.

Schneider, M. E., and D. H. Eggler (1984), Compositions of fluids in equilibrium with peridotite: implications for alkaline magmatism-metasomatism, in Kimberlites. I. Kimberlites and related rocks, edited by J. Kornprobst, pp. 383-394, Elsevier.

Socrates, G. (2001), Infrared and Raman Characteristic Group Frequencies - Tables and Charts, 3 ed., 347 pp., John Wiley & Sons, New York.

Stolen, R. H., and G. E. Walrafen (1976), Water and its relation to broken bond defects in fused silica, Journal of Chemical Physics, 64, 2623-2631.

Stolper, E. (1982), The speciation of water in silicate melts, Geochimica et Cosmochimica Acta, 46, 2609-2620.

Stone, J., and G. E. Walrafen (1982), Overtone vibrations of OH groups infused silica optical fibers, Journal of Chemical Physics, *74*, 1712-1722.

Trevani, L. N., E. C. Balodis, and P. R. Tremaine (2007), Apparent and standard partial molar volumes of NaCl. NaOH, and HCl in water and heavy water at T=523K and 573 K at P=14 MPa, Journal of Physical Chemistry B, 111, 2015-2024.

Veirs, D. K., and G. M. Rosenblatt (1987), Raman line positions in molecular hydrogen - H_2, HD, HT, D_2, DT, and T_2, Journal of Molecular Spectroscopy, 121, 401-409.

Wagner, W., and A. Pruss (2002), The IAPWS formulation 1995 for the thermodynamic properties of ordinary water substance for general scientific use. Journal of Physical Chemistry Reference Data, 31, 387-535.

Walrafen, G. E. (1968), Raman Spectral Studies of HDO in H_2O, Journal of Chemical Physics, 48, 244.

Walrafen, G. E. (1971), Raman spectra from HDO in H_2O to 7.2 kbar, Journal of Physical Chemistry, 55, 5137-5139.

Walrafen, G. E., M. R. Fisher, M. S. Hokmabadi, and W. H. Yang (1986), Temperature dependence of the low- and high-frequency Raman scattering from liquid water. Journal of Chemical Physics, 85, 6970-6982.

Walrafen, G. E., W. H. Yang, Y. C. Chu, and M. S. Hokmabadi (1996), Raman OD-stretching overtone spectra from liquid D_2O between 22 and 152 degrees C, Journal of Physical Chemistry, 100, 1381-1391.

Wang, Y. B., S. X. Cody, G. D. Cody, and B. O. Mysen (2011), ^{2}H and ^{1}H NMR study on hydrogen isotope effects in silicate glasses, in 2011 AGU Fall Meeting, American Geophysical Union, San Francisco, CA.

Williams, K. A., B. K. Pradhan, P. C. Eklund, M. K. Kostov, and M. W. Cole (2002), Raman spectroscopic investigation of H_2, HD, and D_2 physisorption on ropes of single-walled, carbon nanotubes, Physics Review Letters, 88, 165505.

Yoder, H. S., D. B. Stewart, and J. R. Smith (1957), Ternary feldspars, Carnegie Institution of Washington Year Book, 56, 206-214.

Zotov, N., and H. Keppler (1998), The influence of water on the structure of hydrous sodium tetrasilicate glasses, American Mineralogist , 83, 823-834.

Zotov, N., and H. Keppler (2002), Silica speciation in aqueous fluids at high pressures and high temperatures, Chemical Geology, 184, 71-82.

674

This is a preprint, the final version is subject to change, of the American Mineralogist (MSA)
Cite as Authors (Year) Title. American Mineralogist, in press.
(DOI will not work until issue is live.) DOI: http://dx.doi.org/10.2138/am.2013.4449

Table 1. Procedure to calculate NBO/T of a melt†

1. Convert chemical analysis to atomic proportions
2. (a) Establish proportion of tetrahedrally-coordinated cations (T-cations) (b) At pressures below those where pressure-induced coordination changes occur, the main three T-cations are Si^{4+}, Al^{3+}, and P^{5+}. Under certain circumstances, Fe^{3+} and Ti^{4+} may also exist in tetrahedral coordination in silicate melts. †
3. Note that T-cations are assigned a formal charge of 4+. This is accomplished via charge-balance with alkalis or alkaline earths conceptually similar to charge-balance of tetrahedrally-coordinated cations in crystal chemistry.
4 The NBO/T is calculated by electrical charge-balance in which T-cations are assigned a formal charge of 4 and oxygen a formal charge of 2-. With X_T and X_O their proportions from the chemical analysis, the NBO/T of a melt is: $NBO = (2 \bullet X_O - 4 \bullet X_T)/X_T$

† This procedure can only be used provided that melt/glass structural information is available with which to assign cations to tetrahedral coordination.

This is a preprint, the final version is subject to change, of the American Mineralogist (MSA)
Cite as Authors (Year) Title. American Mineralogist, in press.
(DOI will not work until issue is live.) DOI: http://dx.doi.org/10.2138/am.2013.4449

Table 2. Run data

Temp., °C	Press., MPa**	Time, min†	Phases	Raman	FTIR
	Low-density (0.67 g/cm^3)#				
425*	156	N.A.	Melt+Fluid	x††	o##
500	231	65	Melt+Fluid	x	o
575	285	70	Melt+Fluid	x	o
650	405	65	Melt+Fluid	x	x
725	561	75	Melt+Fluid	x	x
800	754	60	Melt+Fluid	x	o
	High-density (0.81 g/cm^3) #				
25	0.1	N.A.	Glass+Fluid	x	x
425	562	70	Melt+Fluid	x	x
500	682	75	Melt+Fluid	x	x
575	876	80	Melt+Fluid	x	x
650	922	75	Melt+Fluid	x	x
725	1079	60	Melt+Fluid	x	x
800	1271	65	Melt+Fluid	x	x

Density is calculated assuming PVT properties of the fluid are the same as pure H_2O (from Wagner and Pruss, 2002).

FTIR spectrum recorded, but melt spectra show clear strong influence of absorption from surrounding aqueous fluid (see text and Fig. 2 for additional details)

* Raman spectrum of ^{13}C diamond was also recorded at room temperature (25°C)

** Uncertainty, which incorporates both the fitting errors of the pressure calibration of the ^{13}C Raman shift (Mysen and Yamashita, 2010) and frequency error in the Raman shift, is ~ 100 MPa. However, precision which incorporates only the frequency error in the Raman shift is ~ 40 MPa.

† Time between attaining the temperature (and pressure) and beginning of recording of spectrum of fluid (which was always recorded before melt).

†† Analyses carried out.

This is a preprint, the final version is subject to change, of the American Mineralogist (MSA)
Cite as Authors (Year) Title. American Mineralogist, in press.
(DOI will not work until issue is live.) DOI: http://dx.doi.org/10.2138/am.2013.4449

Table 3. Enthalpy values from temperature-dependent partitioning (Figs. 8-11)

Partition coefficient	Experiment	ΔH, kJ/mol	Partition coefficient	Experiment	ΔH, kJ/mol
$K_H^{fluid/melt}$	Raman: low-density	-7.6±0.7	$(D/H)^{melt}$	Raman: low-density	0.8±1.3
$K_H^{fluid/melt}$	Raman: high-density	-5.4±1.0	$(D/H)^{melt}$	Raman: high-density	4.0±0.8
$K_H^{fluid/melt}$	FTIR: high-density	-5.1±0.9	$(D/H)^{melt}$	FTIR: high-density	1.8±2.4
$K_H^{fluid/melt}$	Mysen (2013)†	-8.1±3.6	$(D/H)^{melt}$	Mysen (2013)†	2.8±0.9
$K_D^{fluid/melt}$	Raman: low-density	-11.9±0.5	$K_{H/D}^{fluid/melt}$	Raman: low-density	-4.2±0.6
$K_D^{fluid/melt}$	Raman: high-density	-9.7±1.4	$K_{H/D}^{fluid/melt}$	Raman: high-density	5.4±0.7
$K_D^{fluid/melt}$	FTIR: high-density	-9.3±0.8	$K_{H/D}^{fluid/melt}$	FTIR: high-density	-4.8±0.3
$K_D^{fluid/melt}$	Mysen (2013)†	-10.1±2.2	$K_{H/D}^{fluid/melt}$	Mysen (2013)†	-6.4±1.4
$(D/H)^{fluid}$	Raman: low-density	-3.2±0.5			
$(D/H)^{fluid}$	Raman: high-density	-1.4±0.8			
$(D/H)^{fluid}$	FTIR: high-density	-3.0±3.7			
$(D/H)^{fluid}$	Mysen (2013)†	-2.0±2.6			

† Fluid density from Mysen (2013): 0.86 g/cm^3

Figure Captions

Figure 1 – Microphotograph of sample, from high-density fluid experiment, at 800°C and 1271 MPa.

Figure 2 – Schematic representation of infrared beam path through sample in diamond anvil cell with melt globule diameter less than the distance between upper and lower diamond of the diamond anvil cell.

Figure 3 – Eaman spectra of H_2O, recorded in-situ in the HDAC at temperatures and pressures indicated on individual spectra. Micron-sized pieces of Pt was loaded together with the H_2O. The sample was contained in an Ir gasket similar to that used in the other experiments. The H_2O density and pressures at different temperatures were calculated from the PVT data of H_2O (Wagner and Pruss, 2002).

Figure 4 - Pressure/temperature trajectories of the two series of experiments (low- and high-density fluid) with pressure a function of temperature as seen in equations (1a) and (1b). Also shown (dashed lines) is the pressure/temperature trajectory of the experimental series in Mysen (2013). The sharp peak near 900 cm^{-1} in the spectrum of fluid at 425°C/156 MPa is from the CCD response to cosmic rays.

Figure 5 –Examples of Raman spectra of melts in the low-frequency region at temperature and pressure indicated on individual spectra. The sharp peak near 350 cm^{-1} in the spectrum of fluid at 800°C/1271 MPa is from the CCD response to cosmic rays.

Figure 6 – A. Examples of Raman spectra of silicate-saturated (D_2O+H_2O) low-density fluid at temperature and pressure indicated on individual spectra. B. Same as A except from high-density fluid. The sharp peak near 3350 cm^{-1} in the spectrum of melt at 425°C/156 MPa is from the CCD response to cosmic rays.

Figure 7 – Examples of Raman spectra of coexisting water-saturated melt and silicate-saturated fluid from low-density experimemnts at temperatures and pressures indicated on individual spectra.

Figure 8 – Examples of FTIR absorption spectra of coexisting water-saturated melt and silicate-saturated fluid from high-density experimemnts at temperatures and pressures indicated on individual spectra.

Figure 9 – Fluid/melt partition coefficient for hydrogen, measured as total H_2O, $K_H^{fluid/melt}$, as a function of temperature and pressure (as indicated). The pressure scales were calculated from equations (1a) and (1b) based on the Raman shift of ^{13}C diamond (Fig. 4). Error bars reflect progression of errors from calculating the areas of the integrated Raman intensity assigned to OH-stretching in H_2O in the 3000-3700 cm^{-1} frequency range.

Figure 10 – Fluid/melt partition coefficient for deuterium, measured as total D_2O, $K_D^{fluid/melt}$, as a function of temperature and pressure (as indicated). The pressure scales were calculated from equations (1a) and (1b) based on the Raman shift of ^{13}C diamond (Fig. 4). Error bars reflect progression of errors from calculating the areas of the integrated Raman intensity assigned to OD-stretching in D_2O in the 2100-2800 cm^{-1} frequency range.

Figure 11 – A. D/H fractionation factors for fluid, $(D/H)^{fluid}$, based on the OD/OH ratio derived from the Raman and FTIR spectra (as indicated) as a function of temperature. B. D/H fractionation factors for coexisting melt, $(D/H)^{melt}$, based on the OD/OH ratio derived from the Raman and FTIR spectra (as indicated) as a function of temperature.

799 The pressure scales were calculated from equations (1a) and (1b) based on the Raman
800 shift of ^{13}C diamond (Fig. 4). Error bars reflect progression of errors from calculating
801 the areas of the integrated Raman and FTIR absorption intensity assigned to OD-
802 stretching in D_2O and OH in H_2O in Raman and FTIR spectra.
803 Figure 12 – Exchange equilibrium coefficient for coexisting fluid and melt, $K_{D/H}^{fluid/melt}$,
804 as a function of temperature and pressure for experimental series indicated. The
805 pressure scales were calculated from equations (1a) and (1b) based on the Raman shift
806 of ^{13}C diamond (Fig. 4). Error bars reflect progression of errors from calculating the
807 areas of the integrated Raman and FTIR absorption intensity assigned to OD-stretching
808 in D_2O and OH in H_2O in Raman and FTIR spectra from melts and fludis.
809

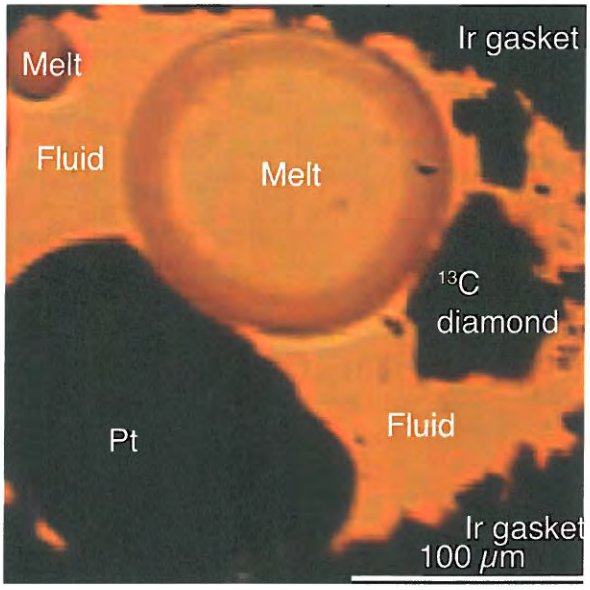
Melt
Ir gasket
Fluid
Melt
^{13}C
diamond
Pt
Fluid
Ir gasket
100 μm

Fig. 1 (4449R1)

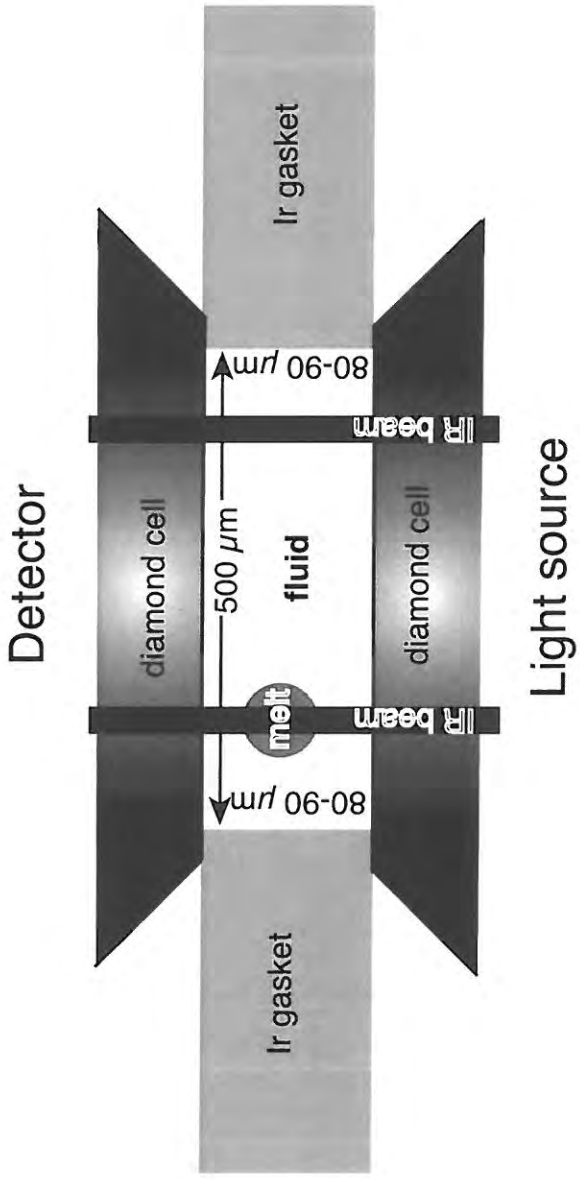
Ir gasket
80-90 μm
IR beam
Detector
diamond cell
500 μm
fluid
melt
diamond cell
Light source
IR beam
80-90 μm
Ir gasket

Fig.2 (4449R1)

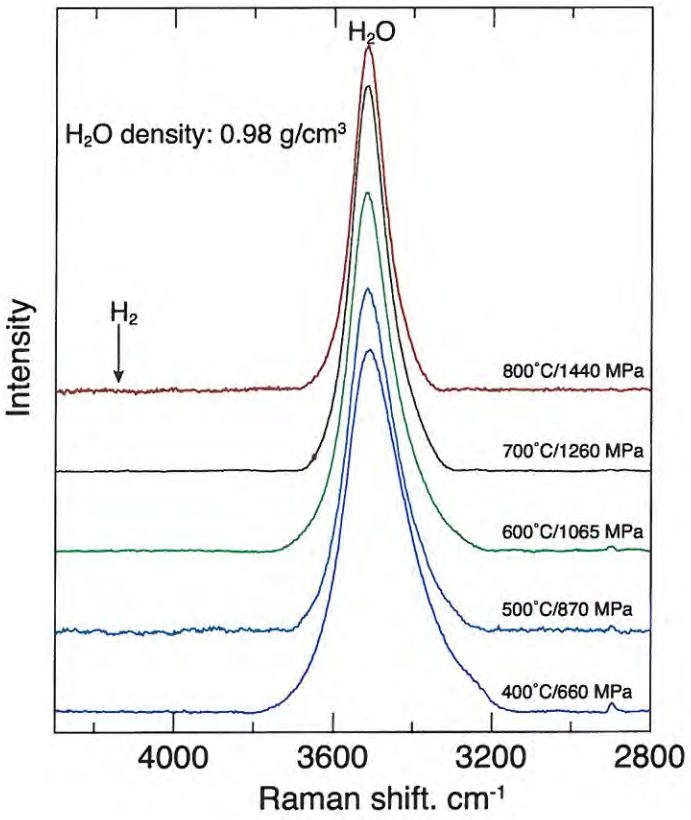
H2O
H2O density: 0.98 g/cm3
H2
Intensity
800°C/1440 MPa
700°C/1260 MPa
600°C/1065 MPa
500°C/870 MPa
400°C/660 MPa
4000
3600
3200
2800
Raman shift. cm-1

Fig. 3(4449R1)

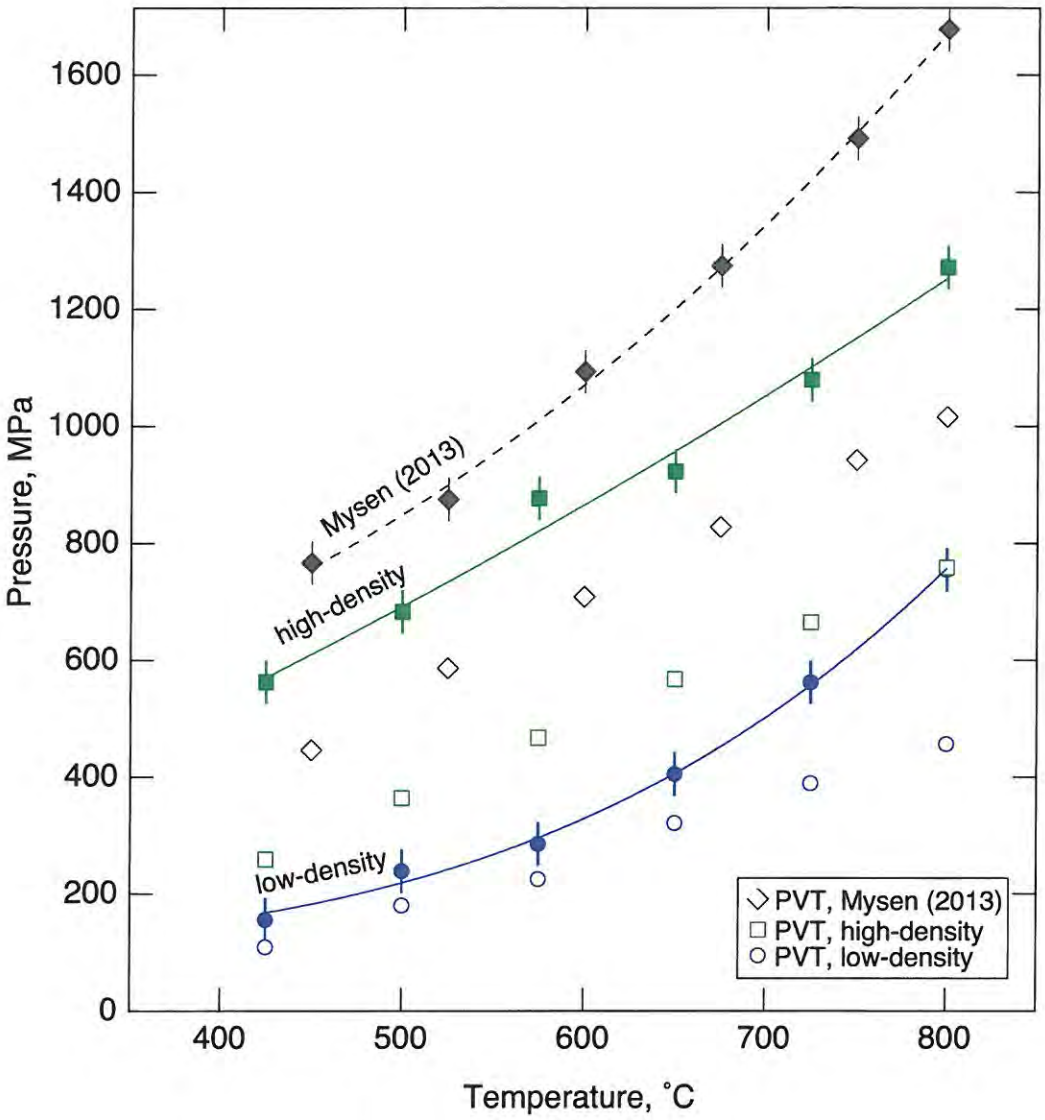
Pressure, MPa
Temperature, ˚C
0
200
400
600
800
1000
1200
1400
1600
400
500
600
700
800
Mysen (2013)
high-density
low-density
PVT, Mysen (2013)
PVT, high-density
PVT, low-density

Fig. 4 (4449R1)

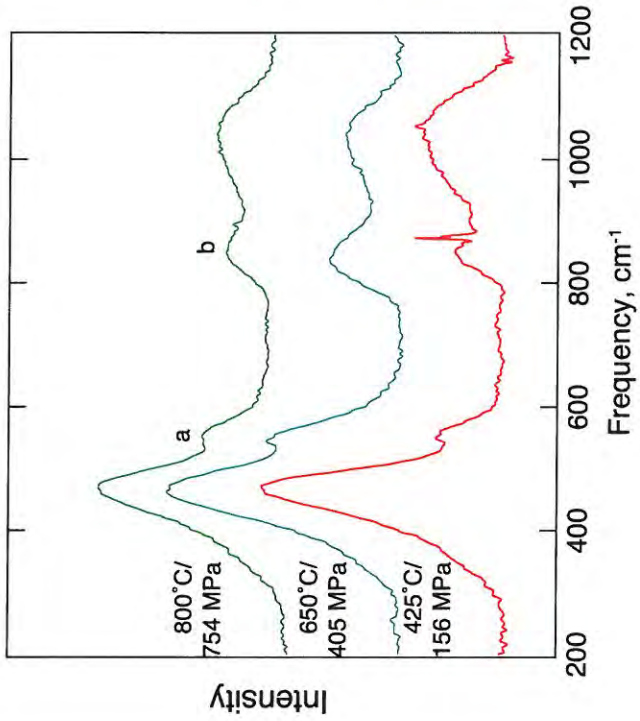
Intensity
200
400
600
800
1000
1200
Frequency, cm-1
800°C/
754 MPa
650°C/
405 MPa
425°C/
156 MPa
a
b

Fig. 5(4449R1)

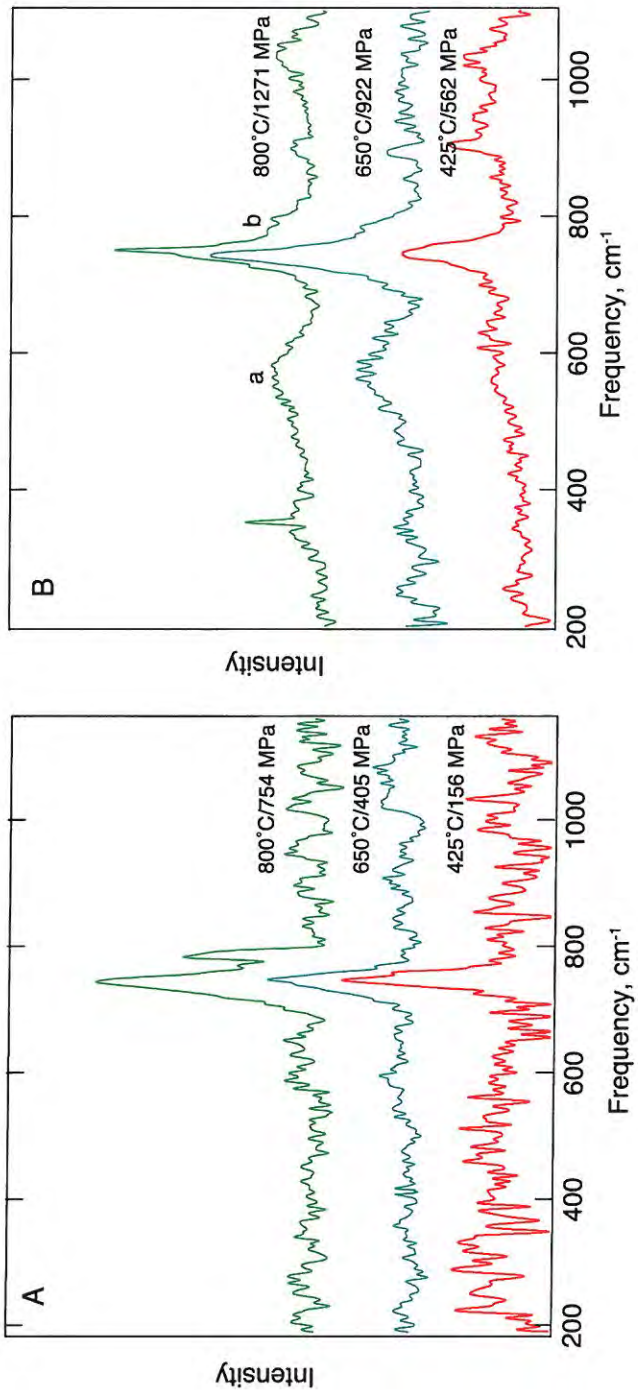
A
800°C/754 MPa
650°C/405 MPa
425°C/156 MPa
Intensity
200
400
600
800
1000
Frequency, cm-1
B
a
b
800°C/1271 MPa
650°C/922 MPa
425°C/562 MPa
Intensity
200
400
600
800
1000
Frequency, cm-1

Fig. 6 (4449R1)

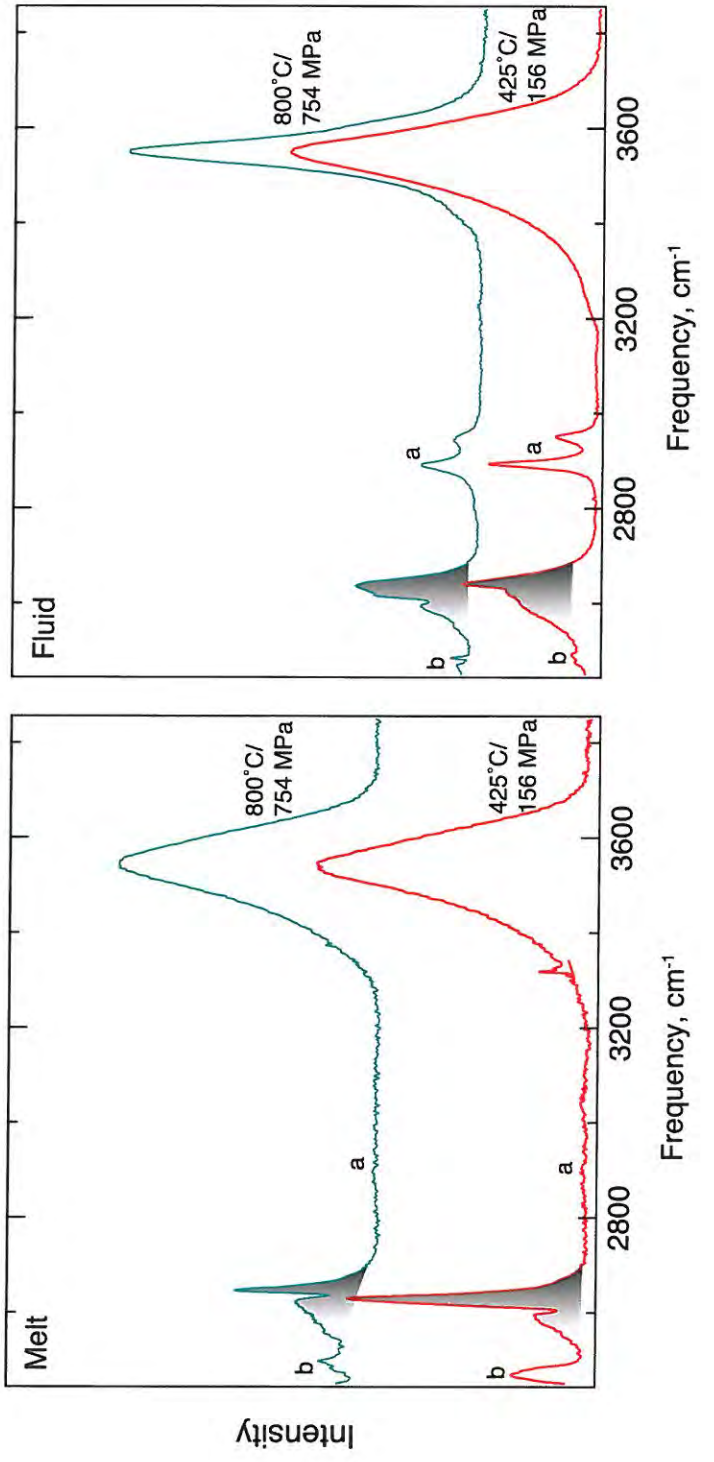
Fluid
Melt
800°C/
754 MPa
425°C/
156 MPa
a
b
2800
3200
3600
Frequency, cm-1
Intensity

Fig. 7(4449R1)

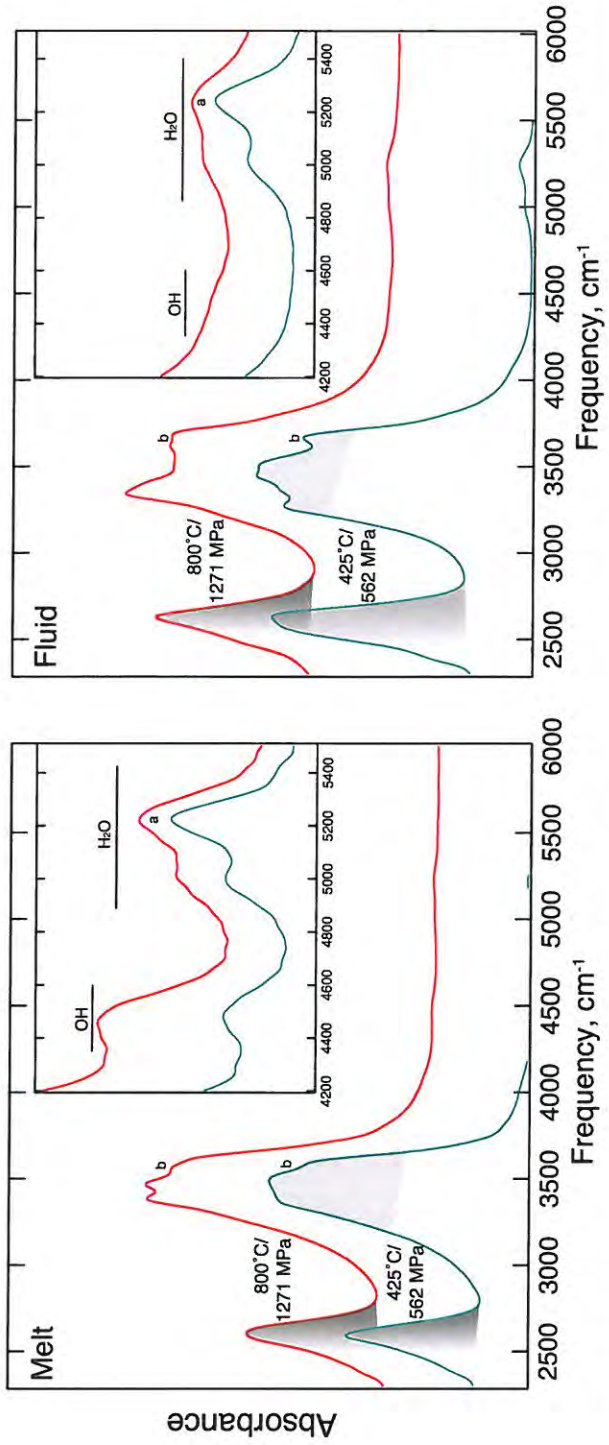
Fluid
Melt
800°C/
1271 MPa
425°C/
562 MPa
OH
H2O
a
b
Absorbance
Frequency, cm-1
2500
3000
3500
4000
4500
5000
5500
6000
4200
4400
4600
4800
5000
5200
5400

Fig. 8 (4449R1)

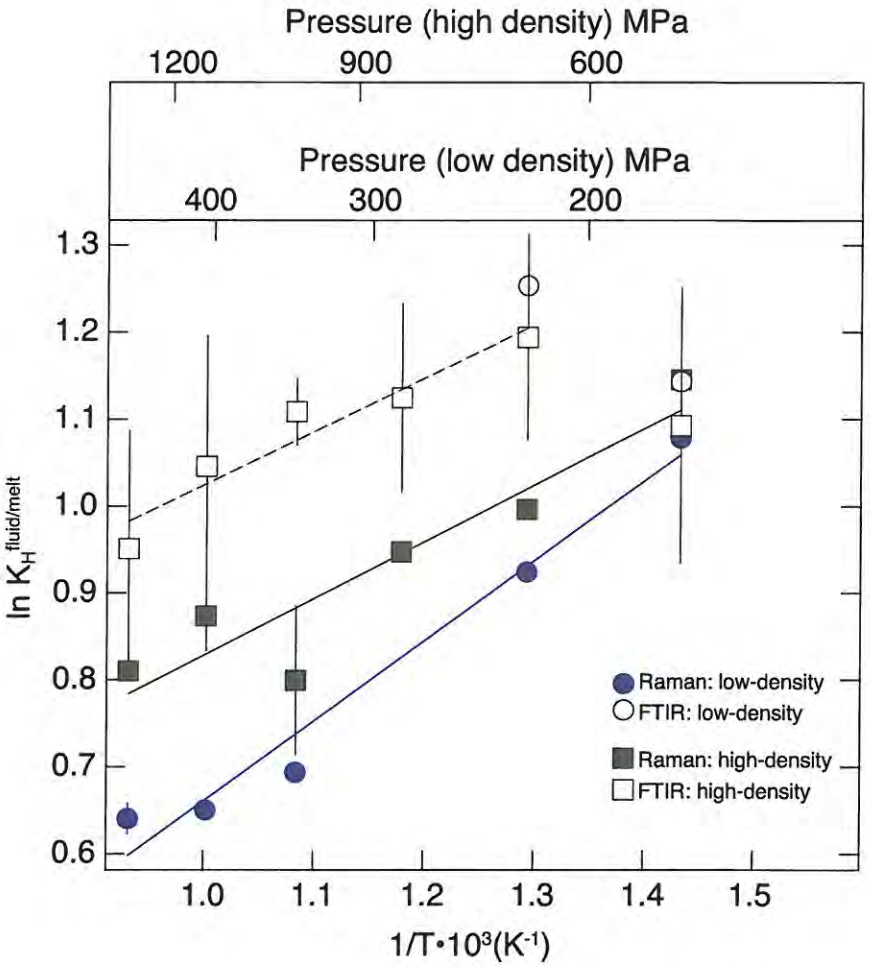
Pressure (high density) MPa
1200
900
600
Pressure (low density) MPa
400
300
200
1.3
1.2
1.1
1.0
0.9
0.8
0.7
0.6
ln $K_H^{fluid/melt}$
Raman: low-density
FTIR: low-density
Raman: high-density
FTIR: high-density
1.0
1.1
1.2
1.3
1.4
1.5
1/T•10³(K⁻¹)

Fig. 9 (4449R1)

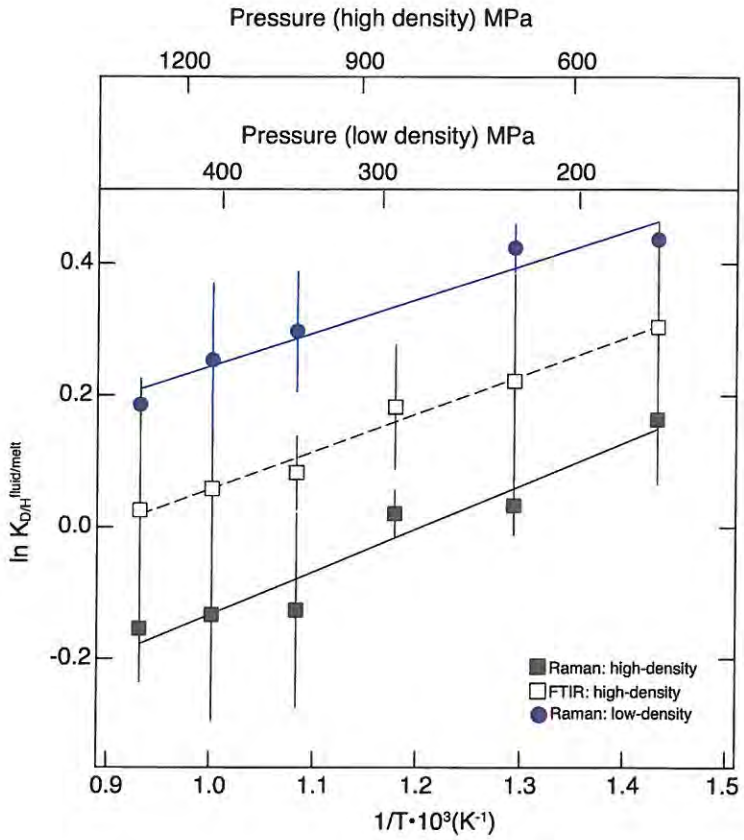

Fig. 12 (4449R1)